



HAL
open science

Anisotropic features of natural Teguline clay

Feng Zhang, Yu Jun Cui, Ling-Ling Zeng, Nathalie Conil

► **To cite this version:**

Feng Zhang, Yu Jun Cui, Ling-Ling Zeng, Nathalie Conil. Anisotropic features of natural Teguline clay. *Engineering Geology*, 2019, 261, p105275. <10.1016/j.enggeo.2019.105275>. <hal-02499355>

HAL Id: hal-02499355

<https://hal.science/hal-02499355v1>

Submitted on 27 May 2021

HAL is a multi-disciplinary open access archive for the deposit and dissemination of scientific research documents, whether they are published or not. The documents may come from teaching and research institutions in France or abroad, or from public or private research centers.

L'archive ouverte pluridisciplinaire **HAL**, est destinée au dépôt et à la diffusion de documents scientifiques de niveau recherche, publiés ou non, émanant des établissements d'enseignement et de recherche français ou étrangers, des laboratoires publics ou privés.



HAL Authorization

34 **Abstract:** In general, due to their geological formation by deposition, natural stiff
35 clays exhibit anisotropic thermo-hydro-mechanical behaviour. This behaviour is
36 important to be considered in geological and geo-environmental engineering. In this
37 study, natural stiff Teguline clay was extracted at different depths and the thermal
38 conductivity, compressibility and hydraulic conductivity were determined on samples
39 along various orientations with respect to the bedding plane. Significant thermal and
40 hydraulic conductivity anisotropies were evidenced with higher values along the
41 bedding plane, indicating that both heat and water transfers preferentially occurred
42 along the direction parallel to the bedding plane. Moreover, the compression index in
43 the horizontal direction were found lower than in the vertical direction, while opposite
44 phenomenon was observed for the yield stress. The degrees of thermal conductivity
45 anisotropy η_T , compression index anisotropy η_{Cc1} , yield stress anisotropy $\eta_{\sigma'_y}$ and
46 hydraulic conductivity anisotropy η_{k1} were found comparable, indicating that bedding
47 is a good indicator of the inherent thermo-hydro-mechanical anisotropy for natural
48 stiff clays. Upon loading in oedometer after the yield stress, the inherent anisotropy
49 changed: for the vertical sample (loading direction normal to the bedding plane),
50 loading led to more and more anisotropy, while for the horizontal sample (loading
51 direction parallel to the bedding plane), the inherent anisotropy disappeared first; then,
52 the induced anisotropy was developed. These findings provided useful information for
53 analyzing the thermo-hydro-mechanical anisotropy of natural soils in geotechnical
54 and geo-environmental engineering.

55 **Key words:** Clays; Anisotropy; Thermal conductivity; Compressibility; Hydraulic

56 conductivity

57

58 **Introduction**

59 Due to their layered microstructure resulting from their initial deposition, natural stiff
60 clays generally exhibit inherent anisotropy, which leads to directional dependence of
61 their thermal, mechanical and hydraulic properties. This anisotropic feature is
62 important to be accounted for while analysing the stability of the galleries excavated
63 for geological nuclear waste disposal (Armand et al., 2013; François et al., 2014;
64 Salehnia et al., 2015; Seyedi et al., 2017), because: i) during excavation, the damage
65 of the host rock (thus the excavation damaged zone) is strongly depending on its
66 anisotropy (Naumann et al., 2007; Niandou et al., 1997; Zhang et al., 2015); ii) after
67 excavation, the stresses exerted to the concrete linings also strongly depend on the
68 anisotropy by the surrounding host rock (Armand et al., 2013). This explains the
69 particular attention paid recently to the anisotropic features of Boom Clay (Dao et al.,
70 2014a; Dao et al., 2014b; Dao et al., 2015a; Dao et al., 2015b), Callovo-Oxfordian
71 claystone (Armand et al., 2013; Zhang et al., 2015; Seyedi et al., 2017) and
72 Tournemire shale (Niandou et al., 1997; Masri et al., 2014), and of Opalinus Clay
73 (Naumann et al., 2007; Bertrand and Collin, 2017; Favero et al., 2018).

74 It has been well documented that for natural clays, the thermal conductivity and
75 hydraulic conductivity in the horizontal direction are in general larger than in the
76 vertical direction (Midttømme and Roaldset, 1999; Dao et al., 2014a), suggesting that
77 the generally horizontal bedding planes are preferential flow directions for heat and
78 fluids. Alshawmar (2014) carried out one-dimensional consolidation tests on
79 undisturbed sensitive Champlain Sea clay and found that the ratio of horizontal to

80 vertical preconsolidation pressure varied from 0.71 to 0.95. Moreover, the horizontal
81 compression index was 1% to 23%, higher than the vertical one, showing a larger
82 compressibility in the horizontal orientation. This can be attributed to the directional
83 differences in soil fabric and in stress history during soil sedimentation (Khan, 1993).
84 The natural clays (such as Opalinus Clay) also exhibited anisotropic features in terms
85 of strength with higher value in the direction parallel and perpendicular to the bedding
86 plane and lower value in the direction at 45° to the bedding plane (Naumann et al.,
87 2007).

88 It is also recognised that the anisotropic hydro-mechanical behavior is directly
89 correlated to the microstructure features (Hicher et al., 2000; Zeng et al., 2017). Zeng
90 et al. (2017) investigated the anisotropic swelling of Teguline clay associated with
91 change in microstructure during wetting. The clay samples were allowed to swell
92 freely or only in the vertical direction. The results showed that swelling occurred
93 mainly in the direction perpendicular to the bedding plane, accompanied with the
94 development of micro-fissures parallel to the bedding plane, the swelling along the
95 bedding direction being negligible. The wetting-induced micro-fissures corresponded
96 to the damage of soil, which could significantly modify the hydro-mechanical
97 properties of soil in an anisotropic fashion.

98 Albeit the importance of anisotropy features recognised for natural soils from
99 both academic and practical points of view, such results remain relatively limited,
100 mainly because of the relatively large variability of natural soils that renders the
101 interpretation of the test results difficult. This study aims at investigating the

102 anisotropy feature of the thermo-hydro-mechanical behaviour of natural clays. Natural
103 Teguline clay was considered for this purpose and its thermal conductivity,
104 compressibility and hydraulic conductivity was determined in various orientations
105 with respect to the bedding plane, which allowed the inherent anisotropy to be
106 identified. Furthermore, the development of stress-induced anisotropy beyond the
107 yield stress was also analyzed.

108

109 **Materials and methods**

110 *Test materials*

111 Stiff Teguline clay samples were extracted from borehole AUB1011 at depths of
112 18.21 m and 31.76 m, also from borehole AUB1012 at depths of 5.46 m, 11.56 m,
113 18.06 m, 30.5 m, 30.8 m and 31.22 m, in the area of Albian Paris Basin (Aube,
114 France), following the direction perpendicular to the bedding plane that was found to
115 be parallel to the ground surface through observation of a piece of Teguline clay
116 immersed in water. They were then covered by membrane and conserved in a fully
117 confined cell (T1), preventing water loss and soil rebounding. This clay has a liquid
118 limit of 42.0-56.5%, a plastic limit of 17.5-29.4% and a specific gravity of 2.71. The
119 mineralogy was mainly defined by illite, illite-smectite, kaolinite, chlorite, quartz and
120 carbonates (Zhang et al., 2018). The clay content and quartz content vary over depth,
121 and their profiles are presented in Fig. 1. It can be observed that Teguline clay consists
122 of 15-60% of clay minerals and 20-70% of quartz. It is worth noting that the tested
123 Teguline clay cores were taken at the depths between 5 m and 40 m. The clay content

124 varied from 35% to 58% and the quartz content from 28% to 46%, showing a certain
125 variability of mineralogy.

126 *Thermal conductivity tests*

127 After opening the Teguline clay from the fully confined cell (T1) in the laboratory,
128 the samples were prepared by trimming to reach the dimensions of 85 mm in diameter
129 and 60 mm - 90 mm in height. Then, they were covered by plastic film to avoid water
130 loss by evaporation. The test program is presented in Table 1.

131 A thermal properties analyzer, KD2, was used to measure the thermal
132 conductivity. Its principle is based on the transient hot-wire method. This device
133 meets the requirements of ASTM Standards (ASTM D5334-00, 2000). In order to
134 install the thermal probe into the soil, a hole was drilled in the centre of each sample.
135 A layer of thermal grease was first applied on the surface of the probe to ensure a
136 good contact between the soil and the probe. Then, the probe with grease was inserted
137 into the sample. The thermal conductivity was measured in three orientations ($\theta = 0^\circ$,
138 $\theta = 90^\circ$, and $\theta = 45^\circ$ to the bedding plane). For a better accuracy, five successive
139 measurements were conducted and a mean value was considered for further analyses.

140 Due to the geological formation by deposition, the Teguline clay is considered as
141 transversely isotropic material. In that case, the measured thermal conductivity λ_0
142 corresponds to that in the direction parallel to the bedding plane $\lambda_{//}$. However, in the
143 case of $\theta = 90^\circ$, the measured thermal conductivity λ_{90} is not the value in the direction
144 perpendicular to the bedding plane (λ_{\perp}). The true value of λ_{\perp} was thus back
145 calculated using the following equation:

146
$$\lambda_{\perp} = \frac{(\lambda_{90})^2}{\lambda_0} \quad (1)$$

147 Eq. (1) has been used by many authors (Penner, 1963; Munroe and Sass, 1987;
 148 Davis et al., 2007; Dao et al., 2014a; Popov et al., 2012; Riche and Schneebeli, 2013;
 149 Ye et al., 2017) to determine the thermal conductivity in the direction perpendicular to
 150 the bedding plane λ_{\perp} in different materials (snow, igneous rocks, clay sediments,
 151 etc.).

152 The thermal conductivity of $\theta=45^{\circ}$ was calculated by Eq. (2) (Dao et al., 2014a):

153
$$\lambda_{45} = \sqrt{\frac{(\lambda_0)^2 + (\lambda_{90})^2}{2}} \quad (2)$$

154 The thermal conductivity of clays depends on the composition (solid, water and
 155 gas phases), the nature of the dominant minerals, the density and temperature (Farouki,
 156 1986; Midttømme and Roaldset, 1999; Tang et al., 2008; Ye et al., 2017). The effect
 157 of the slightly decrease of degree of saturation (S_r) of the studied samples was
 158 accounted for according to the Johansen's method (Johansen, 1975; Farouki, 1986):

159
$$\lambda_{\text{sat}} = \frac{(\lambda - \lambda_{\text{dry}})}{K_e} + \lambda_{\text{dry}} \quad (3)$$

160 where λ_{sat} , λ and λ_{dry} expressed in W/(m·K) are respectively the thermal
 161 conductivities at saturated state, unsaturated state and dry state; K_e is the Kersten's
 162 number.

163 The Kersten's number (K_e) and the thermal conductivity at dry density λ_{dry} can
 164 be determined by the following equations:

165
$$K_e \cong \log(S_r/100) + 1.0 \quad (4)$$

166
$$\lambda_{\text{dry}} = \frac{0.135\rho_d + 64.7}{\rho_s - 0.947\rho_d} \quad (5)$$

167 where S_r is the degree of saturation, ρ_d is the dry unit mass of soil and ρ_s is the unit
 168 mass of solids, both expressed in kg/m^3 .

169 The degree of thermal conductivity anisotropy η_T is defined as:

170
$$\eta_T = \frac{\lambda_{//}}{\lambda_{\perp}} \quad (6)$$

171 where $\lambda_{//}$ (equal to λ_0) and λ_{\perp} were respectively the thermal conductivities in the
 172 directions parallel and perpendicular to the bedding plane.

173 *Compressibility and hydraulic conductivity measurements*

174 The samples extracted from borehole AUB1012 at depths of 11.56 m and 30.5 m,
 175 30.8 m were used for the compressibility and the hydraulic conductivity
 176 measurements. Samples of 50 mm in diameter and 20 mm in height were prepared by
 177 trimming from two directions: horizontal direction and vertical direction. The test
 178 program is presented in Table 2.

179 After installing the soil sample in oedometer cell, step loading was applied up to
 180 the in-situ effective vertical stress without putting the sample in contact with water in
 181 order to avoid soil swelling which would affect the soil microstructure and thereby the
 182 soil hydro-mechanical behavior (Delage et al., 2007; Cui et al., 2013). The in-situ
 183 effective vertical stress σ'_{v0} was estimated using Eq. (7):

184
$$\sigma'_{v0} = \gamma h - u_0$$

185 (7)

186 where γ is the mean unit weight of the soil above the depth considered, h is the depth

187 of the soil core (see Table 2); u_0 is the in-situ pore pressure estimated from the ground
188 water level that is assumed to be at the ground surface for simplicity (Zhang et al.,
189 2018).

190 The value of σ'_{vo} for AUB1012 extracted at 11.56 m was found to be 0.125 MPa.
191 This value was applied to the sample trimmed in the horizontal and the vertical
192 directions (11.56 m). The values of σ'_{vo} for AUB1012 extracted at 30.8 m and 30.5 m
193 were estimated at 0.34 MPa, which was applied to the sample trimmed in the
194 horizontal (30.8 m) and the vertical (30.5 m) directions. It is worth noting that,
195 experimentally, it is difficult to adopt an appropriate stress to be applied to the
196 horizontal sample. Thus, for simplicity, the in-situ effective vertical stress applied to
197 samples in both the horizontal and vertical directions. This also made the comparison
198 between the responses of the samples in two directions easier.

199 After application of σ'_{vo} , the bottom porous stone and the drainage system were
200 saturated with de-ionized water, and the sample was kept saturated for 1 week. Then,
201 a constant water pressure of 0.1 MPa was applied using a controller of
202 pressure/volume (CPV) from the lower base of the cell, and the upper base was kept
203 at atmospheric pressure. Based on the water flux monitored, the hydraulic
204 conductivity was determined by the constant-head method. Afterwards, the injection
205 pressure of 0.1 MPa was reduced to 0.01 MPa, and the compression test was
206 performed in a conventional way by step loading (see Table 2), up to 7.87 MPa for
207 AUB1012 at depth of 11.56 m in two directions and 16.08 MPa for AUB1012 at
208 depths of 30.80 m in the horizontal direction and 30.50 m in the vertical direction.

209 The hydraulic conductivity test was also performed after stabilization at each loading
210 step. The axial displacement was monitored using a LVDT (Linear Variable
211 Differential Transformer), and the deformation was considered as stabilized when the
212 vertical strain rate was lower than 5×10^{-4} every 8 h (AFNOR, 1997). Note that the
213 compression curve of vertical sample (where loading occurred in the direction normal
214 to the bedding plane) from AUB1012 (11.56 m) was collected from Zhang et al.
215 (2018).

216 All the tests were performed at a controlled temperature of $20 \pm 1^\circ\text{C}$.

217

218 **Experimental results**

219 *Thermal conductivity*

220 Since the values of degree of saturation were slightly lower than 100%, the thermal
221 conductivity values at saturated state were first calculated using Eqs. (3), (4) and (5).
222 Figs. 2(a)-2(d) show the changes of thermal conductivity with dry density and water
223 content along the three directions (λ_0 , λ_{45} , λ_{90}) for samples AUB1011 and AUB1012.
224 The calculated values of λ_{45} and λ_{\perp} were also plotted. A good agreement was
225 obtained between calculation and measurement in case of λ_{45} , justifying the
226 calculation method adopted. A significant thermal anisotropy was identified with the
227 highest thermal conductivity values in the direction parallel to bedding, the smallest
228 ones in the direction perpendicular to bedding and the values in-between at 45° . This
229 is consistent with the results reported by Dao et al. (2014a) on Boom Clay: the
230 thermal conductivity in the horizontal direction was found to be higher than in the

231 vertical direction. Moreover, the thermal conductivity along three directions (λ_0 ,
232 λ_{45} , λ_{90}) increased with the increase of dry density (Figs. 2a and 2c), but decreased
233 with the increase of water content (Figs. 2b and 2d). This is commonly explained by
234 the thermal conductivities of soil components (Tang et al., 2008): the thermal
235 conductivity of solids (λ_s is equal to 7.7 W/(m.k) for quartz and 2.0 W/(m.k) for other
236 minerals) is much higher than that of water ($\lambda_w = 0.57$ W/(m.k)). Tang et al. (2008)
237 worked on compacted MX80 bentonite and they also observed that the thermal
238 conductivity increased with the increase of dry density and decreased with the
239 increase of water content.

240 Figs. 3(a)-3(b) show the changes of degree of thermal conductivity anisotropy η_T
241 with dry density and water content for samples AUB1011 and AUB1012. It appears
242 that η_T varied from 1.49 to 1.65 for samples AUB1011 and from 1.23 to 1.55 for
243 samples AUB1012. In addition, the degree of thermal conductivity anisotropy slightly
244 decreased with dry density, but slightly increased with water content.

245

246 *Compressibility and hydraulic conductivity*

247 Fig. 4 presents the compression curves of samples AUB1012 in two directions and at
248 two depths. It can be observed that slight swells occurred during saturation under the
249 in-situ vertical stress σ'_{vo} for the four samples, suggesting that the in-situ stresses were
250 slightly underestimated. By approximating each curve with two straight lines, the
251 compression indexes C_{c1} (corresponding to the common rebounding index C_s) at
252 lower stress and the compression indexes C_{c2} (corresponding to the common

253 compression index C_c) at higher stress were determined. Meanwhile, the yield stresses
254 $\dot{\sigma}_y$ (corresponding to the common pre-consolidation pressure $\dot{\sigma}_p$) were determined as
255 indicated by arrows in the figure. A degree of compression index anisotropy could be
256 then defined either by $\eta_{C_{c1}}$ (ratio of C_{c1} in the vertical direction to C_{c1} in the horizontal
257 direction) or by $\eta_{C_{c2}}$ (ratio of C_{c2} in the vertical direction to C_{c2} in the horizontal
258 direction). Similarly, the degree of yield stress anisotropy $\eta_{\dot{\sigma}_y}$ was defined as the $\dot{\sigma}_y$
259 in the horizontal direction divided by the one in the vertical direction. These
260 parameters are reported in Table 3. The C_{c1} and C_{c2} in the horizontal direction were
261 found to be slightly lower than in the vertical direction, while opposite phenomenon
262 was observed in terms of yield stress. For sample AUB1012 at 11.56 m, the $\eta_{C_{c1}}$ and
263 $\eta_{\dot{\sigma}_y}$ were respectively 2.14 and 1.86, while for sample AUB1012 at 30.5 m and 30.8 m,
264 the two parameters were respectively equal to 2.43 and 2.21. Interestingly, the values
265 of $\eta_{C_{c2}}$ were much lower, close to 1, indicating that after yield, the vertical sample had
266 similar compressibility with the horizontal one.

267 The hydraulic conductivity k of Teguline clay in two directions and at two depths
268 are shown in Fig. 5. For samples at 11.56 m, the logarithm of hydraulic conductivity
269 almost linearly increased with the void ratio in two directions. A significant hydraulic
270 conductivity anisotropy was evidenced, with higher values in the horizontal direction.
271 Further examination showed that for AUB 1012 at 11.56 m, the distance between the
272 lines in two directions gradually decreased after yielding, suggesting that the
273 microstructures of the vertical sample and the horizontal one were getting closer. This
274 phenomenon was not clear for AUB 1012 at 30.50 m and 30.80 m. A degree of

275 hydraulic conductivity anisotropy can be then defined either by η_{k1} (ratio of k_1 in the
276 horizontal direction to k_1 in the vertical direction at the same void ratio) before the
277 yield stress or by η_{k2} (ratio of k_2 in the horizontal direction to k_2 in the vertical
278 direction at the same void ratio) after the yield stress. For samples AUB1012 at 11.56
279 m, the η_{k1} and η_{k2} were respectively 1.73 and 1.5, while for samples AUB1012 at 30.5
280 m and 30.8 m, owing to the limited data before the yield stress in the horizontal
281 direction, only η_{k2} could be determined, which was about 2.0. This hydraulic
282 conductivity anisotropy was also identified on Boom Clay (Yu et al., 2011): a η_{κ} of
283 1.86 was obtained with a hydraulic conductivity in the horizontal direction (6.5×10^{-12}
284 m/s), higher than in the vertical direction (3.5×10^{-12} m/s).

285 In order to investigate the coupling effect between compressibility and
286 permeability, the compression and hydraulic conductivity results are presented
287 together in Fig. 6 in terms of normalized void ratio e/e_0 and normalized hydraulic
288 conductivity k/k_0 versus the logarithm of vertical stress σ'_v for samples AUB1012 at
289 11.56 m (Fig. 6(a)) and AUB1012 at 30.5 m, 30.8 m (Fig. 6(b)). The yield stresses in
290 two directions are also indicated on the compression curves. It can be observed from
291 Fig. 6(a) that: i) the normalized void ratio e/e_0 decreased with the vertical stress σ'_v in
292 two directions and the decrease of e/e_0 in the vertical direction was found to be higher
293 than in the horizontal direction; ii) the normalized k/k_0 decreased with the vertical
294 stress σ'_v in two directions; a linear curve was observed in the vertical direction, while
295 a nearly bi-linear curve was identified in the horizontal direction: when the stress was
296 lower than a threshold stress of 1.91 MPa (higher than the corresponding yield stress

297 of 1.04 MPa), the decrease of k/k_0 was small, and when the stress was higher than
298 1.91 MPa, the decrease of k/k_0 was significantly larger; iii) upon loading below the
299 threshold stress of 1.91 MPa, the decrease of k/k_0 in the horizontal direction was lower
300 than in the vertical direction, which was consistent with the corresponding variation
301 of e/e_0 versus σ'_v ; by contrast, beyond the threshold stress of 1.91 MPa, the decrease
302 of k/k_0 in the horizontal direction was higher than in the vertical direction, which was
303 opposite to the corresponding variation of e/e_0 versus σ'_v , indicating that significant
304 microstructure changes occurred upon loading beyond the threshold stress of 1.91
305 MPa for the horizontal sample. The similar phenomena were observed for the samples
306 at depths 30.5 m and 30.8 m (in Fig. 6(b)).

307

308 **Discussion**

309 *Thermal conductivity*

310 As mentioned previously, quartz has significantly higher thermal conductivity than
311 other minerals. Thus, the global thermal conductivity of soil λ_s is controlled by the
312 volumetric fractions of quartz and other minerals, as follows (Tang et al., 2008):

$$313 \quad \lambda_s = \lambda_q^{v_q} \lambda_o^{1-v_q} \quad (8)$$

314 where λ_q and λ_o are respectively the thermal conductivities of quartz (7.7 W/(m.K))
315 and other minerals (2.0 W/(m.K)). v_q is the volumetric fraction of quartz.

316 The thermal conductivity of soil also depends significantly on the arrangement of
317 particles (McGaw, 1969; Hadley et al., 1984). Many models were used to predict the

318 thermal conductivity (McGaw, 1969; Hadley et al., 1984), among which the series
319 model which assumes perpendicular arrangement of conduction layers and the parallel
320 model which assumes parallel arrangement of conduction layers allowed the lower
321 and upper bounds of thermal conductivities to be defined, as follows:

$$322 \quad \lambda_{series}^{-1} = n\lambda_w^{-1} + (1 - n)\lambda_s^{-1} \quad (9)$$

$$323 \quad \lambda_{parallel} = n\lambda_w + (1 - n)\lambda_s \quad (10)$$

324 where n is the soil porosity; λ_w and λ_s are respectively the thermal conductivities of
325 water and soil solid, expressed in W/(m.K).

326 Fig. 7 presents the comparisons of thermal conductivities between the calculated
327 (using the Eqs. (8), (9) and (10)) and the measured values. It is worth noting that, the
328 measured λ_0 and calculated λ_{\perp} (using Eq. (1) based on the measured λ_0 and λ_{90}) were
329 considered as the measured values in the directions parallel and perpendicular to the
330 bedding plane, respectively. In the calculation, the thermal conductivities of quartz,
331 other minerals and water were taken equal to 7.7 W/(m.K), 2.0 W/(m.K) and 0.57
332 W/(m.K), respectively (Tang et al., 2008). The volumetric fractions of quartz, clay
333 content were determined from Fig. 1 and the soil porosities were calculated from the
334 dry densities (in Table 1). All results of samples AUB1011 and AUB1012 are
335 considered in the analysis. The thermal conductivity results in Fig. 7(a) show that the
336 series model gave satisfactory results, in particular while considering the quartz effect.
337 On the contrary, the parallel model gave underestimation without considering the
338 quartz effect and gave overestimation with consideration of quartz effect.

339 Basically, in case of series model, heat flow took place through water, quartz and
340 other minerals in series in the direction perpendicular to the bedding plane. In that
341 case as less solid contacts could be expected, a lower thermal conductivity was
342 obtained. In the case of parallel model, heat flow took place through water quartz and
343 other soil minerals in the direction parallel to the bedding plane. As more solid
344 contacts were involved in that case, a higher thermal conductivity was expected. The
345 satisfactory results given by the series model with consideration of quartz effect (in
346 Fig. 7(a)) suggests that the volumetric fraction of quartz was important to be
347 accounted for. However, it appears that the parallel model with consideration of the
348 quartz effect overestimated the thermal conductivity (in Fig. 7(b)); thus in that case it
349 seems more suitable to not consider the quartz effect. In fact, the real soil arrangement
350 was neither fully in series, nor fully in parallel. Thus, in the case of series model the
351 consideration of quartz effect compensated the effect of soil particles and water that
352 are not in series, while in the case of parallel model the non-consideration of quartz
353 effect compensated to some extent the effect of soil particles and water that are not in
354 parallel.

355

356 *Compressibility and hydraulic conductivity*

357 Basically, compression in oedometer obeys K_0 condition. The value of K_0 can be
358 estimated using the following equation (Della Vecchia et al., 2010; Lima et al., 2011;
359 Zhang et al., 2018):

$$360 \quad K_0^{SC} = (1 - \sin \varphi') \sqrt{\text{OCR}} \quad (11)$$

361 where K_o^{SC} is the earth pressure coefficient at rest for over-consolidation soil, ϕ' is the
362 effective internal friction angle, OCR is the over-consolidation ratio. For Teguline
363 clay extracted at 11.56 m and 30.5 m, the OCRs are respectively 4.5 and 5.3
364 (determined from Fig. 4), and the effective internal friction angle ϕ' is about 27.3°
365 (Zhang et al., 2018). The K_o^{SC} values determined using Eq. (11) are respectively 1.15
366 and 1.24 for samples extracted at 11.56 m and 30.5 m, indicating that the maximum
367 effective stress that Teguline clay had suffered in the horizontal direction in the
368 history was expected to be higher than in the vertical direction. This is the reason why
369 the yield stress in the horizontal direction was higher than in the vertical direction.

370 The degrees of anisotropy identified in terms of thermal conductivity,
371 compression index, yield stress and hydraulic conductivity are not far from each other
372 for the studied Teguline clay: η_T varied from 1.23 to 1.65, η_{Ccl} from 2.14 to 2.43, η_{σ_y}
373 from 1.86 to 2.21 and η_{kl} was 1.73. This indicates that bedding is a good indicator of
374 thermo-hydro-mechanical anisotropy for natural stiff clays.

375 The compression curves (see Fig. 4) and hydraulic conductivities (see Fig. 5) in
376 the horizontal and the vertical directions were found to gradually converge after yield,
377 suggesting that the hydro-mechanical anisotropy of the horizontal sample was
378 approaching that of the vertical one. As the microstructure of soil does not change
379 significantly before the yield stress, the anisotropy identified represents the inherent
380 one. On the contrary, significant microstructure change can be expected beyond the
381 yield stress and in that case any anisotropy identified represents the induced one.
382 Thereby, the large values of η_{Ccl} , η_{σ_y} and η_{kl} obtained suggest a significant inherent

383 anisotropy of Teguline clay, in agreement with the results of thermal conductivity.
384 Upon loading beyond the yield stress, similar values of compression index $C_{\alpha 2}$ in two
385 directions (see Table 3) were obtained. This does not indicate an isotropic behaviour;
386 it just suggests that the microstructures of the vertical sample and the horizontal one
387 were getting closer after yielding. The evolution of microstructure for vertical and
388 horizontal Teguline clay samples during loading can be described in Fig. 8. For the
389 vertical sample, loading in oedometer after the yield stress led to more and more
390 anisotropic microstructure feature because of the expected increase of particle
391 orientation (Delage and Lefebvra, 1984; Cui et al., 2013), while for the horizontal
392 sample, the inherent anisotropy disappeared first upon loading; then, induced
393 anisotropy developed with the increase of particle orientation. Thus, the changes of
394 principle stresses (as if rotation of principal stresses took place) was involved in that
395 case and the horizontal sample experienced changes from initial inherent anisotropy
396 to isotropy and then to the stress-induced anisotropy.

397 The microstructure changes during loading for vertical and horizontal samples
398 described in Fig. 8 were in agreement with the evolution of k/k_0 with σ'_{v0} in
399 semi-logarithmic plot (Figs. 6(a) and 6(b)). For the horizontal sample, the decrease of
400 k/k_0 with σ'_v was small before the threshold stress, as the fluid flow in the direction
401 parallel to the bedding is dominant and in that case the bedding plane acts as
402 preferential path for water flow. By contrast, beyond the threshold stress, dramatic
403 decrease of k/k_0 was observed, indicating that inherent anisotropy disappeared and
404 induced anisotropy appeared with the increase of particle orientation. In that case,

405 water flow in the direction normal to the induced orientated particles became
406 prevailing. Thereby, for the horizontal sample, the threshold stress identified in the
407 $k/k_0 - \dot{\sigma}_v$ curve in semi-logarithmic plot separated the zone with prevailing parallel
408 flow (in the direction parallel to the inherent bedding plane) from the zone with
409 prevailing perpendicular flow (in the direction perpendicular to the induced orientated
410 particles). This threshold stress should correspond to the stress that generated the
411 isotropic state in the soil. For the vertical sample, no clear threshold stress was
412 observed in the $k/k_0 - \dot{\sigma}_v$ curve in semi-logarithmic plot. This is logical because loading
413 in oedometer after the yield stress led to more and more anisotropy and in that case
414 the changes of perpendicular flow (in the direction perpendicular to the bedding plane
415 before the yield stress and normal to the induced orientated particles after the yield
416 stress) were dominant.

417

418 **Conclusion**

419 The anisotropy feature of stiff Teguline clay was investigated in terms of thermal
420 conductivity, compressibility and hydraulic conductivity. The results obtained allow
421 the following conclusions to be drawn.

422 A significant thermal conductivity anisotropy was evidenced: the highest value
423 was in the direction parallel to the bedding plane and the smallest one in the direction
424 perpendicular to the bedding plane, the one at 45° being logically in between, in
425 agreement with the results of hydraulic conductivity. The compression index also
426 revealed the anisotropic feature of Teguline clay: lower values were identified in the

427 horizontal direction. Moreover, the clay anisotropy was also characterized by higher
428 values of yield stress in the horizontal direction than in the vertical direction.

429 The degrees of thermal conductivity anisotropy η_T , compression index
430 anisotropy η_{Cc1} , the yield stress anisotropy η_{σ_y} and hydraulic conductivity anisotropy
431 η_{k1} were not far from each other, suggesting that bedding is a good indicator of the
432 inherent thermo-hydro-mechanical anisotropy for natural stiff clays.

433 Upon loading in oedometer, the inherent anisotropic features of Teguline clay
434 changed after the yield stress: for the vertical sample, loading led to more and more
435 particle orientation and thus more and more anisotropy. On the contrary, for the
436 horizontal sample, loading led to the disappearance of the inherent anisotropy first,
437 before creating the stress-induced anisotropy. The evolution of k/k_0 versus σ'_{vo} in
438 semi-logarithmic plot also was found to be in agreement with the microstructure
439 changes.

440 These findings confirm that natural stiff clays, through their formation by
441 deposition, develop orientated microstructure. As a result, anisotropic features
442 develop in terms of thermal conductivity, compressibility and hydraulic conductivity.
443 These anisotropic features changed upon loading beyond the yield stress or the
444 threshold stress. This anisotropy feature is important to be accounted for when
445 constructing geotechnical and geo-environmental structures in natural stiff clays.

446

447 **References**

448 AFNOR., 1997. Sols: reconnaissance et essais. Essais oedométriques. Partie 1: Essai
449 de compressibilité sur matériaux fins quasi saturés avec chargement par paliers.

450 Alshawmar, F., 2014. Evaluation of compressibility, anisotropy and at-rest lateral
451 earth pressure in Champlain Sea clays. Master thesis, University of Ottawa.
452 Ottawa, Canada.

453 Armand, G., Noiret, A., Zghondi, J., Seyedi, D.M., 2013. Short- and long-term
454 behaviors of drifts in the Callovo-Oxfordian claystone at the
455 Meuse/Haute-Marne Underground Research Laboratory. *J Rock Mech Geotech*
456 *Eng.* 5, 221-230.

457 ASTM D5334-00, 2000. Standard test methods for determining of thermal
458 conductivity of soil and soft rock by thermal needle probe procedure. ASTM
459 International, West Conshohocken, PA.

460 Bertrand, F., Collin, F., 2017. Anisotropic modelling of Opalinus Clay behaviour:
461 From triaxial tests to gallery excavation application. *J Rock Mech Geotech Eng.*
462 9(3), 435-448.

463 Cui, Y.J., Nguyen, X.P., Tang, A.M., Li, X.L., 2013. An insight into the
464 unloading/reloading loops on the compression curve of natural stiff clays. *Appl.*
465 *Clay Sci.* 83-84, 343-348.

466 Davis, M.G., Chapman, D.S., Van Wagoner, T.M., Armstrong, P.A., 2007. Thermal
467 conductivity anisotropy of metasedimentary and igneous rocks. *J. Geophys. Res.*
468 112 (B05216), 1-7.

469 Dao, L.Q., Delage, P., Tang, A.M., Cui, Y.J., Pereira, J.M., 2014a. Anisotropic thermal
470 conductivity of natural Boom Clay. *Appl. Clay Sci.* 101, 282-287.

471 Dao, L.Q., Cui, Y.J., Tang, A.M., Pereira, J.M., Li, X.L., Sillen, X., 2014b.
472 Investigating the anisotropy of the shear modulus of natural Boom Clay.
473 *Geotech Lett.* 4, 98-101.

474 Dao, L.Q., Cui, Y.J., Tang, A.M., Delage, P., Li, X.L., Sillen, X., 2015a. Anisotropy in
475 Oedometer Test on Natural Boom Clay. *Engineering Geology for Society and*
476 *Territory.* 6, 499-502.

477 Dao, L.Q., Cui, Y.J., Tang, A.M., Pereira, J.M., Li, X.L., Sillen, X., 2015b. Impact of
478 excavation damage on the thermo-hydro-mechanical properties of natural Boom
479 Clay. *Eng Geol.* 195, 196-205.

480 Delage, P., Lefebvre, G., 1984. Study of the structure of a sensitive Champlain clay
481 and of its evolution during consolidation. *Can. Geotech J.* 21(1), 21-35.

482 Delage, P., Le, T.T., Tang, A.M., Cui, Y.J., Li, X.L., 2007. Suction and in-situ stresses
483 of deep Boom clay samples. *Géotechnique.* 57(1), 239-244.

484 Della Vecchia, G., Lima, A., Jommi, C., and Romero, E. 2010. Some remarks on the
485 hydro-mechanical constitutive modelling of natural and compacted Boom clay.
486 *Proc. 5th Int. Conf. on Unsaturated Soils.* Barcelona. Taylor and Francis Group,
487 London, 803-809.

488 Farouki, O.T., 1986. Thermal properties of soils. *Rock and Soil Mechanics* 11. Trans
489 Tech Publications, Clausthal-Zellerfeld, Germany.

490 Favero, V., Ferrari, A., Laloui, L., 2018. Anisotropic behaviour of Opalinus Clay
491 through consolidated and drained triaxial testing in saturated conditions. *Rock*
492 *Mech Rock Eng.* 51(5), 1305-1319.

493 Francois, B., Labiouse, V., Dizier, A., Marinelli, F., Charlier, R., Collin, F., 2014.

494 Hollow Cylinder Tests on Boom Clay: Modelling of Strain Localization in the
495 Anisotropic Excavation Damaged Zone. *Rock Mech Rock Eng.* 47, 71-86.

496 Hadley, G.R., Mcvey, D.F., Morinl, R., 1984. Thermophysical properties of deep
497 ocean sediments. *Marine Geotechnology.* 5(3-4), 257-295.

498 Hicher, Y.P., Wayudi, H., Tessier, D., 2000. Microstructural analysis of inherent and
499 induced anisotropy in clay. *Mech Cohes-frict Mat.* 5(5), 341-371.

500 Johansen, O., 1975. Thermal conductivity of soils. Ph.D. thesis, Trondheim, Norway.
501 (CRREL Draft Translation 637, 1977). ADA 044002.

502 Khan, M.M.A., 1993. Strength-deformation behaviour of a weathered clay crust. PhD
503 thesis, University of Ottawa, Ottawa, Canada.

504 Lima, A., Romero, E., and Piña, Y. 2011. Water retention properties of two deep
505 Tertiary clay formations within the context of radioactive waste disposal. VII
506 Brazilian Symposium on Unsaturated Soil. Pirenópolis, Goiania, Brazil,
507 315-321.

508 Masri, M., Sibai, M., Shao, J.F., Mainguy, M. 2014. Experimental investigation of the
509 effect of temperature on the mechanical behavior of Tournemire shale. *Int J Rock
510 Mech Min Sci.* 70, 185-191.

511 Mcgaw, R., 1969. Heat conduction in saturated granular materials. High research
512 board sepcial report. 103, 114-131.

513 Midttømme, K., Roaldset, E., 1999. Thermal conductivity of sedimentary rocks:
514 uncertainties in measurement and modeling. *Geol. Soc. Lond., Spec. Publ.*
515 158(1), 45-60.

516 Munroe, R.J., Sass, J.H., 1987. Thermal Conductivity of Samples From Borehole
517 VC-1, Report 87-184. Geological Survey.

518 Naumann, M., Hunsche, U., Schulze, O., 2007. Experimental investigations on
519 anisotropy in dilatancy, failure and creep of Opalinus Clay. *Phys. Chem. Earth.*
520 32(8-14), 889-895.

521 Niandou, H., Shao, J.F., Henry, J.P., Fourmaintraux, D., 1997. Laboratory
522 investigation of the mechanical behaviour of Tournemire shale. *Int J Rock Mech
523 Min Sci.* 34(1), 3-16.

524 Penner, E., 1963. Anisotropic thermal conduction in clay sediments. International
525 Clay Conference.

526 Popov, Y., Bayuk, I., Parshin, A., Miklashevskiy, D., Novikov, S., Chekhonin, E.,
527 2012. New methods and instruments for determination of reservoir thermal
528 properties. Proceedings Thirty-seventh Workshop on Geothermal Reservoir
529 Engineering. Stanford University, Stanford, California.

530 Riche, F., Schneebeli, M., 2013. Thermal conductivity of snow measured by three
531 independent methods and anisotropy considerations. *The Cryosphere.* 7,
532 217-227.

533 Salehnia, F., Collin, F., Li, X.L., Dizier, A., Sillen, X., Charlier, R., 2015. Coupled
534 modeling of Excavation Damaged Zone in Boom clay: Strain localization in rock
535 and distribution of contact pressure on the gallery's lining. *Comput Geotech.* 69,
536 396-410.

537 Seyedi, D.M., Armand, G., Noiret, A., 2017. "Transverse Action"- A model

538 benchmark exercise for numerical analysis of the Callovo-Oxfordian claystone
 539 hydromechanical response to excavation operations. *Comput Geotech.* 85,
 540 287-305.

541 Tang, A.M., Cui, Y.J., Le, T.T., 2008. A study on the thermal conductivity of
 542 compacted bentonites. *Appl. Clay Sci.* 41, 181-189.

543 Ye, W.M., Lu, Y., Huang, X.H., Chen, B., Chen, Y.G., Cui, Y.J., 2017. Anisotropic
 544 thermal conductivity of unsaturated compacted GMZ bentonite-sand mixture.
 545 *PanAm Unsaturated Soils.* 413-424.

546 Yu, L., Gedeon, M., Wemaere, I., Marivoet, J., De Craen, M., 2011. Boom clay
 547 hydraulic conductivity. A Synthesis of 30 Years of Research. External Report
 548 SCK-CEN, Mol (Belgium).

549 Zhang, C.L., Armand, G., Conil, N., 2015. Investigation on the anisotropic
 550 mechanical behaviour of the Callovo-Oxfordian clay rock. Final report.

551 Zhang, F., Cui, Y.J., Zeng, L.L., Robinet, J.C., Conil, N., Talandier, Jean., 2018. Effect
 552 of degree of saturation on the unconfined compressive strength of natural stiff
 553 clays with consideration of air entry value. *Eng. Geol.* 237, 140-148.

554 Zeng, L.L., Cui, Y.J., Conil, N., Zghondi, J., Armand, G., Talandier, J., 2017.
 555 Experimental study on swelling behaviour and microstructure changes of natural
 556 stiff clays upon wetting. *Can. Geotech J.* 54(5), 700-709.

557
 558
 559
 560

561 **List of Tables**

562 **Table 1.** Program for thermal conductivity tests
 563 **Table 2.** Program for compressibility and hydraulic conductivity tests
 564 **Table 3.** Parameters obtained from the compression curves
 565

566 **List of Figures**

567 **Fig. 1.** Variations of (a) clay content; (b) quartz content over depth
 568 **Fig. 2.** Variations of thermal conductivity with (a) dry density for samples AUB1011;
 569 (b) water content for samples AUB1011; (c) dry density for samples AUB1012; (d)
 570 water content for samples AUB1012
 571 **Fig. 3.** Variations of degree of thermal conductivity anisotropy η_T with (a) dry density;
 572 (b) water content
 573 **Fig. 4.** Compression curves
 574 **Fig. 5.** Hydraulic conductivity k versus void ratio e
 575 **Fig. 6.** Normalized e/e_0 or k/k_0 versus vertical stress σ'_{v0} for samples (a) AUB1012 at
 576 11.56 m; (b) AUB1012 at 30.5 m and 30.8 m
 577 **Fig. 7.** Comparisons of measured thermal conductivity and calculated values by (a)

578 series model; (b) parallel model

579 **Fig. 8.** Conceptual model for vertical sample and horizontal sample subjected to
580 loading in one-dimensional condition

581
582
583
584
585
586
587
588
589
590
591
592
593
594
595
596
597
598
599
600
601
602
603

Table 1. Program for thermal conductivity tests

Core	Depth(m)	Water content (%)	Dry density (Mg/m ³)	Direction
AUB1011	18.21	13.68	1.98	0° , 45° and 90°
	31.76	12.13	2.04	0° , 45° and 90°
AUB1012	5.46	19.53	1.74	0° , 45° and 90°
	11.56	15.28	1.87	0° , 45° and 90°
	18.06	14.69	1.90	0° , 45° and 90°
	30.5	12.20	2.04	0° , 45° and 90°
	31.22	12.19	2.06	0° , 45° and 90°

604
605

606

Table 2. Program for compressibility and hydraulic conductivity tests

Core	Depth(m)	Direction	Stress path (MPa)
AUB1012	11.56	Horizontal	0.125-0.375-0.874-1.874-3.872-7.869
		Vertical	
	30.8	Horizontal	0.345-0.594-1.094-2.093-4.092-8.089-16.083
		Vertical	
30.5	Vertical		

607

Note that the horizontal direction refers to the loading direction parallel to the bedding

608

plane, while the vertical direction refers to the loading direction normal to the bedding

609

plane.

610

611

Table 3. Parameters obtained from the compression curves

Core	Direction	C_{C1}	η_{Cc1}	$\dot{\sigma}_y$	$\eta_{\dot{\sigma}_y}$	C_{C2}	η_{Cc2}
AUB1012 11.56 m	Horizontal	0.0081		1.04		0.074	
	Vertical		2.14		1.86		1.09
AUB1012 30.8 m	Horizontal	0.0042		3.97		0.064	
	Vertical		2.43		2.21		1.14
AUB1012 30.5 m	Vertical	0.0102		1.80		0.073	

612

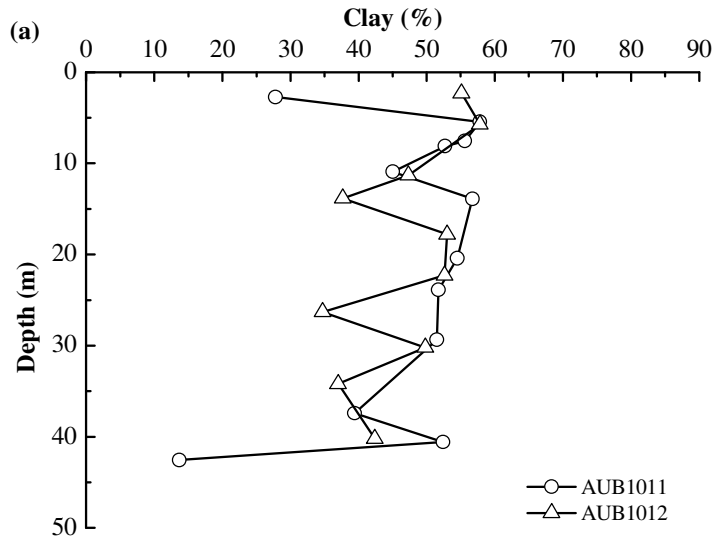
613

614

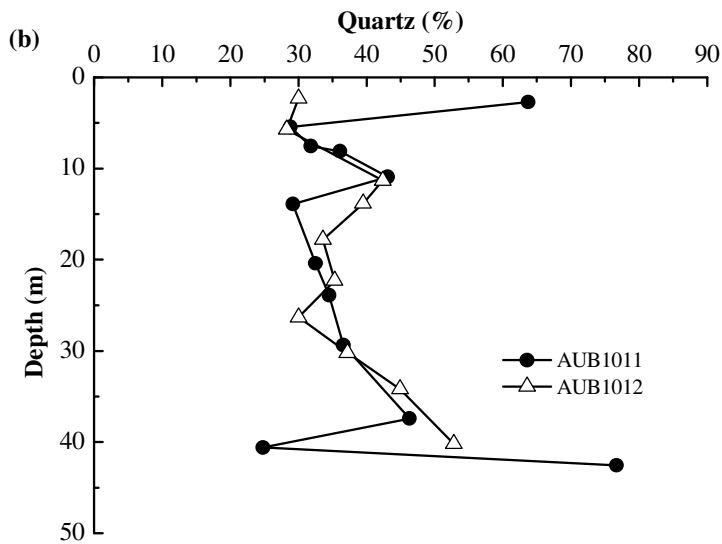
615

616

617



618

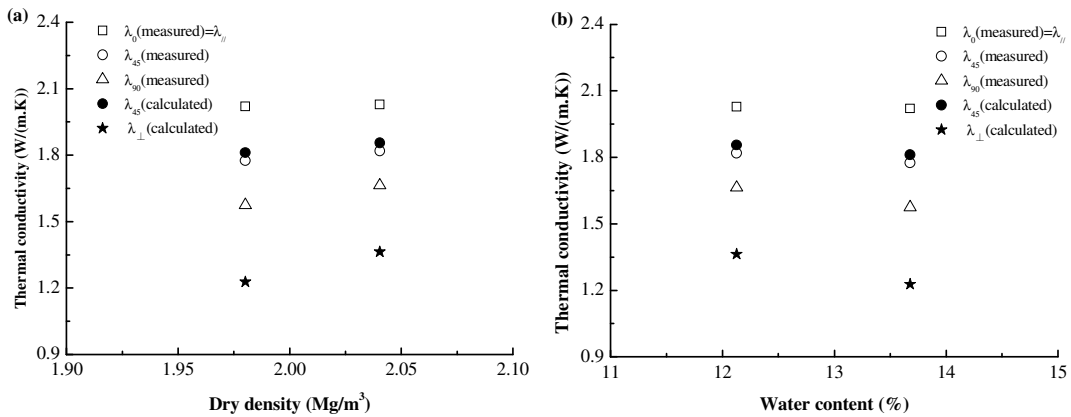


619

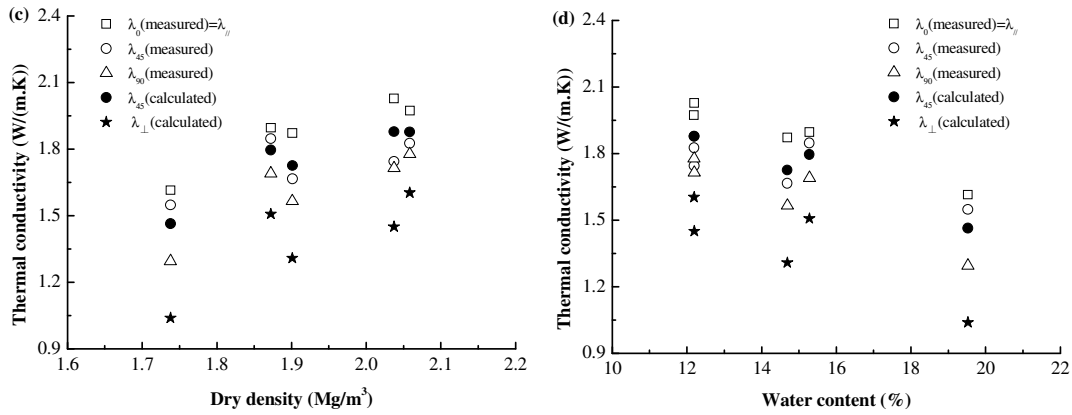
620

Fig. 1. Variations of (a) clay content; (b) quartz content over depth

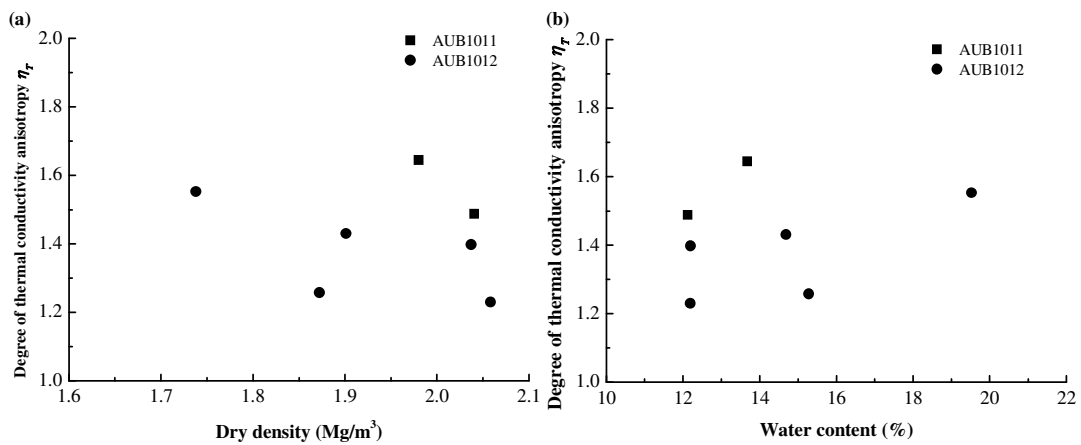
621



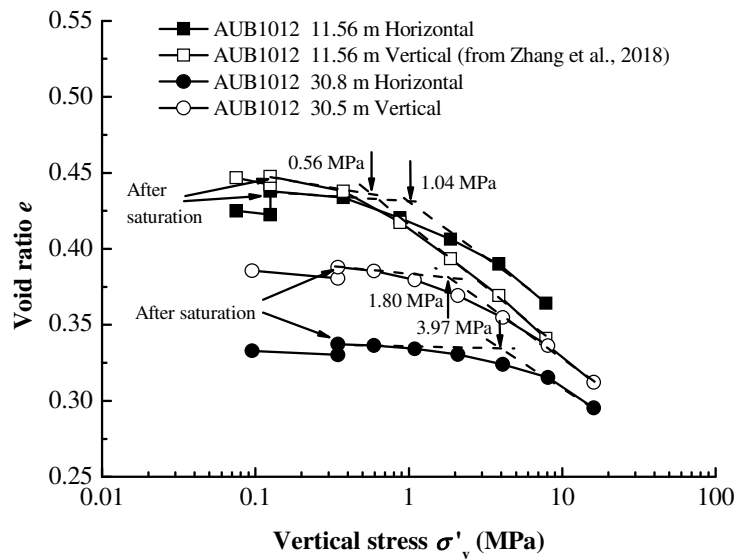
622



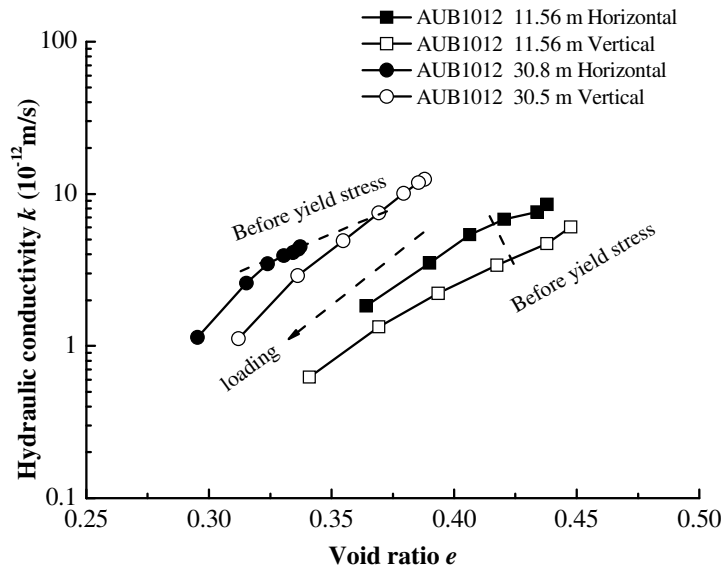
623
 624 **Fig. 2.** Variations of thermal conductivity with (a) dry density for samples AUB1011;
 625 (b) water content for samples AUB1011; (c) dry density for samples AUB1012; (d)
 626 water content for samples AUB1012



627
 628 **Fig. 3.** Variations of degree of thermal conductivity anisotropy η_T with (a) dry density;
 629 (b) water content



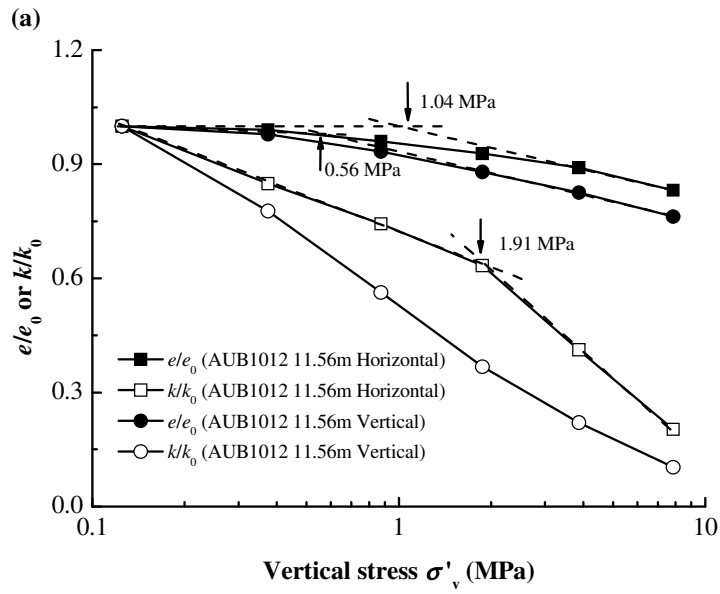
630
 631 **Fig. 4.** Compression curves



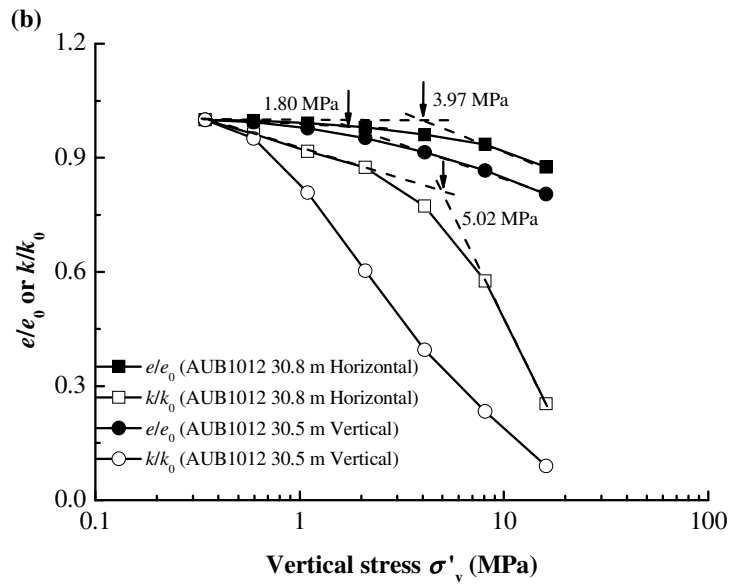
632

633

Fig. 5. Hydraulic conductivity k versus void ratio e

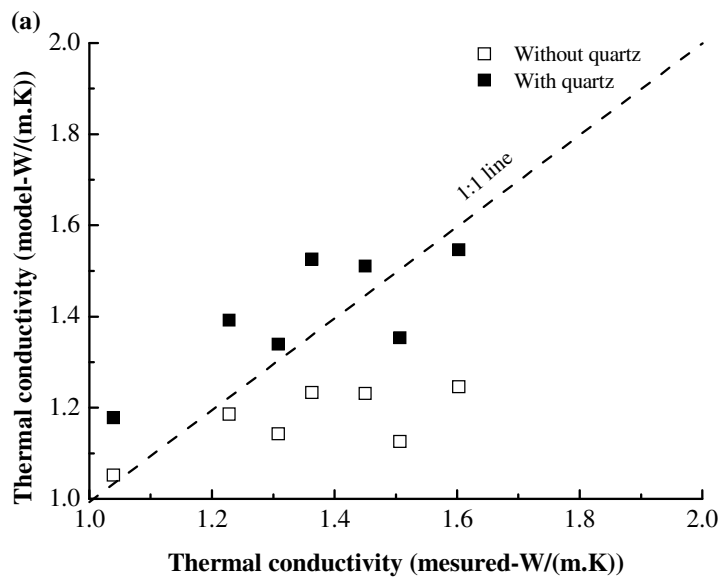


634

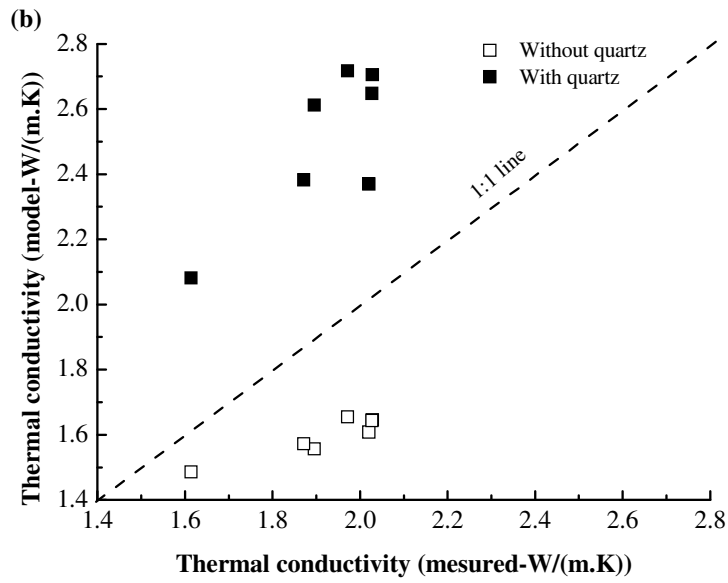


635

636 **Fig. 6.** Normalized e/e_0 or k/k_0 versus vertical stress σ'_{v0} for samples (a) AUB1012 at
 637 11.56 m; (b) AUB1012 at 30.5 m and 30.8 m

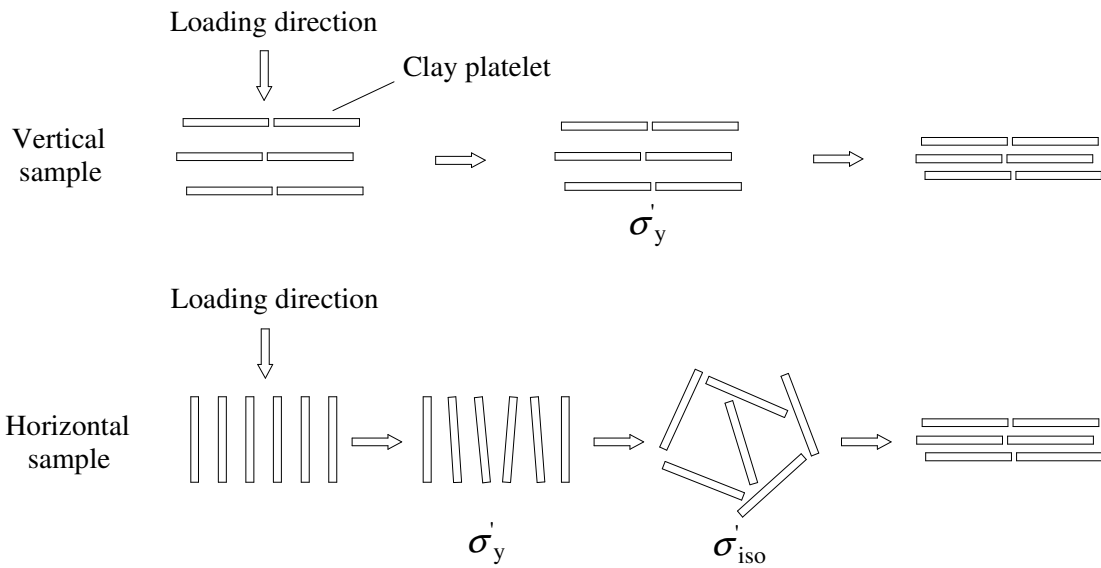


638



639
640
641
642

Fig. 7. Comparisons of measured thermal conductivity and calculated values by (a) series model; (b) parallel model



643
644
645
646

Fig. 8. Conceptual model for vertical sample and horizontal sample subjected to loading in one-dimensional condition